HHS Public Access

Author manuscript

Nat Methods. Author manuscript; available in PMC 2014 December 01.

Published in final edited form as:

Nat Methods. 2014 June ; 11(6): 677–682. doi:10.1038/nmeth.2928.

High-density single-molecule analysis of cell surface dynamics in *C. elegans* embryos

Francois B. Robin[1], **William M. McFadden**[1,3], **Baixue Yao**[1], and **Edwin M. Munro**[1,2,4]

[1]Department of Molecular Genetics and Cell Biology, University of Chicago, Chicago, Il, 60637

[2]Institute for Biophysical Dynamics, University of Chicago, Chicago, Il, 60637

[3]Biophysics Graduate Program, University of Chicago, Chicago, Il, 60637

[4]Computation Institute, University of Chicago, Chicago, Il, 60637

Abstract

We describe a general, versatile and non-invasive method to image single molecules near the cell surface that can be applied to any GFP-tagged protein in *C. elegans* embryos. We exploit tunable expression via RNAi and a dynamically exchanging monomer pool to achieve fast continuous single-molecule imaging at optimal densities with signal-to-noise ratios adequate for robust single particle tracking (SPT) analysis. We also introduce and validate a new method called smPReSS that infers exchange rates from quantitative analysis of single molecule photobleaching kinetics, without using SPT. Combining SPT and smPReSS allows spatially and temporally resolved measurements of protein mobility and exchange kinetics. We use these methods (a) to resolve distinct mobility states and spatial variation in exchange rates of the polarity protein Par-6 and (b) to measure spatiotemporal modulation of actin filament assembly and disassembly. The introduction of these methods in a powerful model system offers a promising new avenue to investigate dynamic mechanisms that pattern the embryonic cell surface.

Introduction

Dynamic remodeling of the embryonic cell surface is essential for the control of cell polarity, division, shape change and movement during early development. This remodeling involves the dynamic interplay of local exchange and movement of proteins that reside at the interface between the plasma membrane and the actin-rich cell cortex. However, quantifying these processes in embryonic cells remains a significant challenge. One

Corresponding author: emunro@uchicago.edu.

Author Contributions

EMM conceived the imaging approach and provided overall guidance. FBR conceived and developed smPReSS approach, and with EMM, developed the tracking based turnover analysis. FBR and WMC acquired the data for Actin, BY and FBR acquired the data for PAR-6, WMM, FBR and BY performed the non-linear fitting, EMM, FBR, BY and WMM developed and performed the mobility analysis. FBR performed the tracking-based turnover analysis, FBR, WMM, BY and EMM made the figures. EMM and FBR wrote the text.

Competing financial interests

The authors declare no competing financial interests.

promising approach is single-molecule imaging combined with single particle tracking (SPT), which can yield quantitative measurements of local mobilities, binding states and exchange kinetics that are inaccessible to ensemble measurements[1–3]. Combining these approaches with powerful genetic tools in a classical model organism could be a powerful way to investigate subcellular dynamics in embryonic cells, but this has yet to be achieved.

One key limitation has been the lack of simple and reliable methods for tunable and non-invasive labeling of target molecules. Optimal labeling densities are different for each target and must balance the need for high-density sampling of molecular behavior in space and time against practical requirements for accurate and unbiased single molecule detection and tracking. Methods based on microinjection of fluorescently labeled probes[4,5], or transfection using crippled promoters[6–9] are cumbersome and inherently hard to optimize. Methods based on surface labeling of transmembrane proteins[10–13] may be easier to tune, but cannot be generalized to intracellular targets. A more promising approach for intracellular targets uses genetically encoded photoswitchable fluorescent protein fusions to create a renewable supply of single molecules[14–16], However, this approach does not report on spatiotemporal variations in density or assembly/binding kinetics of the endogenous protein. Moreover, its use in *C. elegans* would require de novo creation of a transgenic strain for each new target of interest.

Here we describe a simple, versatile and minimally invasive method for single-molecule imaging at the cell surface in *C. elegans* embryos that can be applied to any of the large and growing collection of transgenic strains expressing GFP-tagged fusion proteins[17]. We combine sequence-specific inhibition of GFP transgene expression with selective photobleaching and simple in vivo standards to achieve and verify single-molecule densities of GFP-fusions over normal levels of the endogenous protein. We exploit the intrinsic exchange dynamics of surface-associated proteins to obtain long term (>5000 frames) sampling of single molecule trajectories at signal-to-noise ratios (SNR), frame rates and densities that can be optimized to measure local mobility and turnover for a given molecule. In particular, we show how these data can be used to extract quantitative information about surface density and turnover through two complementary methods: The first involves direct inference from single particle trajectories. The second method, which we refer to as smPReSS for single-molecule Photobleaching Relaxation to Steady State, estimates turnover rates by fitting simple kinetic models to measurements of single-molecule densities over time and is therefore insensitive to particle tracking errors. To demonstrate the power of this approach, we quantify spatiotemporal variations in mobility and turnover for the polarity protein Par-6 and for actin filaments during asymmetric cell division in the one-cell *C. elegans* embryo.

Results

Obtaining and verifying single-molecule levels

In *C. elegans*, a 200nm thick eggshell[18,19] makes it difficult to image subsurface dynamics with true TIRF optics. To overcome this, we used near-TIRF illumination[20], optimizing laser angle and intensity to achieve ~even illumination across the field of view while maintaining adequate SNR for robust single particle detection and tracking (Fig. 1a;

Supplementary Fig. 1; Online Methods). For any given transgenic strain expressing GFP fused to a target protein, we used a two-step method to achieve densities of GFP-tagged proteins suitable for single-molecule imaging (Fig. 1b). First, we directed RNA interference (RNAi) against the GFP sequence to selectively reduce maternal expression of the transgene, yielding presumably low levels of GFP-tagged protein over normal levels of the endogenous protein. For more than a dozen strains tested, we could readily tune exposure times to obtain transgene expression levels at which diffraction limited-speckles could be observed at the cell surface by near-TIRF microscopy (Fig. 1c). In a second step, we used photobleaching to further reduce speckle densities (#speckles.μm^{-2}) and mean speckle intensity towards single-molecule levels (Fig. 1d), with no adverse consequences for cell viability (**see Online Methods**).

Next we established a general method to verify single-molecule levels for any GFP fusion strain that can be readily extended across labs and imaging platforms. We focused on polarity maintenance phase in the one-cell embryo when the distributions of many surface proteins are essentially stationary. Concentrating initially on a strain expressing GFP fused with Actin (GFP::Actin), we reduced transgene levels as above until the average intrinsic speckle intensity ($I_{int} = I_{speckle} - I_{background}$) reached a minimum value and the distribution of intensities was well-fit by a single Gaussian (Fig. 1d). Then we imaged at high laser power such that speckle disappearance was dominated by photobleaching, rather than disassembly. Under these conditions, the majority of disappearance events occurred in single-steps, confirming that the minimum intensity speckles we observe correspond to single GFP molecules (Fig. 1e). Strikingly, when we reduced expression levels in 5 other GFP fusion strains to minimize the mean speckle intensity, we measured speckle intensity distributions during maintenance phase that were indistinguishable from one another and from those measured for GFP::Actin under the same imaging conditions (Fig. 1f). Moreover, by fitting multiple Gaussians (for 1,2,…N fluorophores/particle) to the distribution of I_{int}, we could readily detect when more than 5% of speckles contained multiple fluorophores (Fig. 1d, Supplementary Fig. 2,3a). Thus for any given strain, it is possible to pinpoint a characteristic speckle density below which a “pure” population of single molecules can be reliably observed, which can subsequently be used to calibrate single-molecule imaging on other platforms.

Long term single-molecule imaging of mobility and turnover

We sought to exploit the intrinsic exchange dynamics of surface-associated proteins to create a self-renewing pool of GFP-tagged single molecules at the cell surface that could be followed over time to measure mobility and turnover. To establish a kinetic basis for this approach, we consider a GFP-tagged protein that exchanges dynamically between the bulk cytoplasm and a region of the cell surface, which is observed by near-TIRF microscopy (Fig. 2a). The number of molecules *N(t)* within this region over time is governed by:

$$\frac{dN}{dt} = k_{app} - (k_{off} + k_{ph}) \cdot N \quad (1)$$

where k_{app} is an observable appearance rate that depends on the cytoplasmic concentration of GFP-tagged protein ($k_{app} = k_{on} \times Y$, where Y is the cytoplasmic concentration) and the

nature of the binding process, and k_{off} and k_{ph} are pseudo-first order rate constants such that $k_{off} \times N$ is the rate (in molecules per second) at which particles disappear due to unbinding or disassembly, and $k_{ph} \times N$ is the rate (in molecules per second) at which they disappear due to irreversible photobleaching. (Fig. 2a). Prior to illumination, $k_{ph} = 0$ and the steady state density is $N_{ss} \sim \frac{k_{app}}{k_{off}}$. During illumination, k_{ph} becomes non-zero; if the cytoplasmic pool were infinite, the system would approach a new steady state density given by $N_{ss}^{obs} = \frac{k_{app}}{k_{off}+k_{ph}}$, which is a fixed fraction $f = \frac{k_{off}}{k_{off}+k_{ph}}$ of the initial unobserved value (Fig. 2b). In practice, irreversible photobleaching will gradually deplete a finite cytoplasmic pool. A variant of the kinetic model that accounts for this depletion (see **Online Methods**) predicts a biphasic response to the onset of illumination: a fast relaxation towards $\sim N_{ss}^{obs}$, followed by a slower decay towards 0, at a rate which depends on the photobleaching rate and the size of the cytoplasmic pool (Fig. 2b, Supplementary Note 1). For a given target molecule, k_{off} is fixed. However, k_{ph} depends on imaging conditions (i.e. the intensity and duty ratio of the laser illumination, while k_{app} can be adjusted by tuning the initial size of the GFP-tagged pool. Thus by co-tuning these factors, it should be possible to target a desired density N_{ss}^{obs} at quasi-steady state for a range of imaging conditions.

To test this approach, we chose two representative strains expressing GFP::Actin and PAR-6::GFP. Actin monomers exchange dynamically with the cell surface through local filament assembly and disassembly, and based on previous work, we expected GFP::F-Actin to be relatively immobile at the cell surface and to turn over in a few 10s of seconds[21], while fast-diffusing monomers of GFP::Actin should produce highly blurred images and thus escape detection under our imaging conditions[6]. Par-6 is a conserved polarity protein that binds dynamically to sites on the plasma membrane[22–24] and recent FRAP measurements suggest that it diffuses rapidly at the cell surface and dissociates very slowly[25], with an effective dissociation rate constant $k_{off} = 5.4 \pm 5 \times 10^{-3}\ s^{-1}$. Focusing again on polarity maintenance phase, we reduced densities to single-molecule levels, allowed the system to equilibrate unobserved, and then recorded data for a range of laser intensities and exposure times (Fig. 2c–e, Supplementary Fig. 2,3b). For both strains, we observed the predicted biphasic response to a step change in illumination – a rapid initial decrease in the number of molecules to a quasi-stable value followed by slower decay (Fig. 2c,d, Supplementary 2,3a, also Supplementary Video 1). Importantly, the initial decrease was reversed with equally rapid kinetics when the laser was turned off (Fig. 2c) confirming that the quasi-steady state is set by a dynamic balance of exchange and photobleaching. For both strains, we could therefore obtain robust estimates for effective dissociation and photobleaching rate constants k_{off} and k_{ph}, by fitting the predicted biphasic kinetics to the change in single-molecule density over time; for each strain, we optimized fitting conditions by adjusting laser exposure (intensity and duty ratio; see below and Supplementary Note 2). As expected, estimates of k_{ph} varied linearly with laser exposure while estimates of k_{off} remained fixed over a range of exposures (Fig. 2f). Significantly, our estimates of k_{off} for Par-6 in the anterior cortex ($k_{off} = 7.4 \pm 0.7 \times 10^{-3}\ s^{-1}$) are consistent with those previously obtained by FRAP ($k_{off} = 5.4 \pm 5 \times 10^{-3}\ s^{-1}$, ref. 25). We refer to this approach as smPReSS for single-molecule Photobleaching Relaxation to Steady State. Because smPReSS relies directly on

counting single molecules, it is relatively insensitive to non-specific fluorescence and can be applied at very low fluorophore densities that would be inaccessible using ensemble methods like FRAP and its variants. Moreover, because it does not rely on particle tracking, it is insensitive to particle tracking errors.

Next, we assessed the potential for long-term high-density sampling of single molecule trajectories, as previously achieved with photoswitchable fluorophores. To this end, we set laser intensities to ensure signal-to-noise ratios and frame rates suitable for robust particle tracking using standard SPT algorithms and software[26,27] (Supplementary Video 1–3, **Online Methods**, Supplementary Table 1). Under these conditions, we measured effective photobleaching rate constants $k_{ph} \sim 0.1\ s^{-1}$ for GFP::Actin and $k_{ph} \sim 0.3\ s^{-1}$ for PAR-6::GFP, resulting in less than 30% loss in density over 5000 frames (Fig. 2d, Supplementary Fig. 2, 3a). When we pre-tuned the initial size of the cytoplasmic pool to optimize quasi-stable densities towards maximal values consistent with robust SPT, we were able to recover for GFP::Actin (resp. PAR-6::GFP) ~30,000 (resp. ~7,500) individual trajectories over the 5000-frame interval, with an average duration of 35 (resp. 15) frames, and ~5000 (resp. ~250) trajectories lasting longer than 80 frames. We observed comparable results with several other strains (data not shown). Thus, the intrinsic exchange dynamics of GFP-tagged proteins can be exploited to achieve continuous long-term single-molecule imaging, and these imaging conditions can be tuned to optimize single particle tracking analysis or estimates of bulk turnover by smPReSS.

SPT analysis reveals distinct classes of Par-6 mobility

The ability to rapidly sample large numbers of individual trajectories makes it possible to analyze surface dynamics during well-defined and short-lived windows of developmental time. To illustrate this, we tracked local movements of PAR-6::GFP molecules at the cell surface during maintenance phase in one-cell embryos. To get a rough classification of Par-6 mobilities, we measured mean-square-displacement (MSD) vs lag time t for 1086 trajectories with lifetimes larger than 80 frames (Fig. 3a,b). Then we fit the first 10 time points to $MSD = 4Dt^{\alpha}$ to estimate the anomalous diffusion exponent α and a short-term diffusivity D. This analysis revealed what appears to be at least two distinct mobility classes (Fig. 3b,c, Supplementary Video 1,4,5). Approximately 43% of Par-6 molecules undergo what appears to be simple diffusion, with $0.9<\alpha<1.2$ and short term diffusivity $D = 0.17 \pm 0.10\ \mu m^2.s^{-1}$ (Fig. 3b,c), which is comparable to previous measurements by FRAP ($0.28 \pm 0.05\ \mu m^2.s^{-1}$, ref. 25). Another ~22% of Par-6 molecules undergo what appears to be slower sub-diffusive motion, with $\alpha<0.6$ and short term $D = 0.008 \pm 0.008\ \mu m^2.s^{-1}$ (Fig. 3b,c). The remaining 35% of the tracks undergo intermediate behavior, with short term $D = 0.057 \pm 0.032\ \mu m^2.s^{-1}$ for $0.6 \leq \alpha \leq 0.9$ (Fig. 3b,c). Simulating Brownian diffusion with diffusivities chosen randomly from the range $D = 0.15 \pm 0.05\ \mu m^2.s^{-1}$ and then analyzing trajectories as above reproduced a distribution of short term D and alpha values very similar to the distribution observed for the subset of real particles with $0.9<\alpha<1.2$ (Fig. 3d). In contrast (and as expected) for no values of D did simulated Brownian diffusion reproduce the class of trajectories for $\alpha<0.6$ observed for single molecules of Par-6 (Supplementary Fig. 4). These observations are consistent with previous studies documenting two populations of Par-6, punctate and diffuse, with distinct localizations and genetic requirements, and which

likely reflect different binding modes and binding partners for Par-6[22]. Further analyses combining the sampling methods introduced here with e.g. Bayesian trajectory analysis[28,29] and genetic manipulation should yield further information about these different binding states and their regulation.

Measuring spatio-temporal variations in density/turnover

A key advantage of our approach is that the GFP-tagged proteins sample the same kinetics as the underlying pool. Thus, they report not just on mobilities, but also on spatiotemporal variation in densities, appearance rates (k_{app}) and per molecule turnover rates (k_{off}). In principle, k_{app} and k_{off} can be measured either directly from single molecule trajectories or by smPReSS as described above. However practical considerations constrained the choice of method as illustrated by analysis of Par-6 turnover during polarity maintenance and actin turnover during cell division.

Measuring spatial variation of Par-6 turnover

Par-6 is highly enriched at the anterior cortex in polarized one-cell embryos. These differences are thought to be caused by more rapid dissociation of Par-6 in the posterior[30]. However, anterior vs posterior differences in dissociation rate cannot be detected by conventional FRAP analysis because the densities of Par-6 in the posterior are too low. Unfortunately, the photobleaching rates ($k_{ph} \sim 0.3\ s^{-1}$) required for accurate particle tracking are ~40-fold higher than the dissociation rates ($k_{off} = 7.4 \pm 0.7 \times 10^{-3}\ s^{-1}$) measured by smPReSS. Thus resolving A vs P differences in turnover by particle tracking would be difficult or impossible because photobleaching will dominate small differences in k_{off}. Instead, we exploited the tunability of our approach, setting laser exposure and image acquisition (100% laser, 30ms exposure at 1 second intervals) to maintain accurate detection while reducing photobleaching rates to $k_{ph} \sim 0.005$. Under these conditions, smPReSS yielded robust estimates of k_{off} for anterior and posterior regions ($k_{off}^{ant} = 7.4 \pm 0.7 \times 10^{-3}\ s^{-1}$, $k_{off}^{post} = 7.4 \pm 0.7 \times 10^{-3}\ s^{-1}$). Combined with measurements of relative density ($N_{ant}/N_{post} = 9.0 \pm 1.4$), this allowed us to infer relative values for k_{app} ($k_{off}^{ant}/k_{off}^{post} = 7.2 \pm 2.0$). Interestingly, our results suggest that the majority of the A vs P difference in density is due to differences in recruitment rates, consistent with the enrichment of several known binding partners for Par-6 (Cdc-42 and Par-3) at the anterior[31,22].

Modulation of actin assembly/turnover during cell division

As a second example, we measured spatiotemporal modulation of actin assembly and disassembly during the first cell division (Fig. 4a, Supplementary Video 2,3). Both actin assembly and disassembly are thought to be modulated during cytokinesis[32], but their relative contributions to actin filament accumulation are not well understood. We performed these experiments in embryos depleted of non-muscle Myosin II to remove the confounding effects of surface deformations and flow and remove myosin-dependent effects on turnover[33,34]. We verified strong depletion of Myosin II by the complete failure of cytokinesis and a complete absence of local surface deformation and cortical flow during early anaphase. In the case of GFP::Actin, the turnover rates measured by smPReSS ($k_{off} \sim 0.1\ s^{-1}$) were similar to the photobleaching rates ($k_{ph} \sim 0.1\ s^{-1}$) required for accurate particle

tracking, and agreed well with estimates of k_{off} from particle tracking (Fig. 4b; Supplementary Fig. 5), suggesting that in this case, we could use SPT to measure spatiotemporal variations in turnover, using the smPReSS measurements of k_{ph} to correct for photobleaching. We measured roughly uniform values for k_{app} and k_{off} along the AP axis during maintenance phase (Fig. 4c–e), consistent with a lack of cortical asymmetry at this stage in myosin-depleted embryos (data not shown). During the transition into anaphase, when the contractile ring normally assembles, we observed a net increase in actin density at the equator as anticipated, and we also observed a net decrease at the poles (Fig. 4a,c). Surprisingly, these changes involved strong modulation of both filament assembly and disassembly (Fig. 4d,e). The equatorial increase was associated with a small increase in assembly rate and a larger decrease in turnover, while the polar decrease in density was associated with both a decrease in assembly and an increase in turnover. Thus our ability to simultaneously resolve assembly, disassembly and density revealed an unappreciated dimension to the control of cortical microfilaments during cell division.

Discussion

Here we describe for the first time a simple and tunable method to monitor single molecule mobility and exchange dynamics at the cell surface in embryonic cells of a genetic model organism – *C. elegans*. By tuning the size of the GFP-tagged pool and photobleaching rates, we obtained continuous long term sampling of single molecule trajectories at densities and track lengths that are limited mainly by the photostability of GFP and by well-known constraints on the accurate detection and tracking of single molecules. We focused here on single-molecule imaging and analysis. However brighter (multi-molecule) speckles may be optimal for some analyses[35], and can be readily achieved through a slightly different tuning of the cytoplasmic pool. Our approach is minimally invasive because it relies on sampling very low levels of GFP fusions over normal levels of the endogenous protein, with no detectable phototoxicity, even at very high laser power. Because we rely on the intrinsic exchange of GFP fusion proteins between the cytoplasm and the cell surface, no additional methods or reagents are required to target fluorophores to the protein of interest, and the method can be readily implemented by anyone with access to a TIRF microscope equipped for GFP excitation and a sufficiently sensitive (e.g. back-thinned EM-gain CCD) camera. Our approach thus leverages the large collection of existing fusion strains in *C. elegans*[17], plus recently developed methods for the rapid production of new strains by genome editing[36], and can be readily combined with any of the large arsenal of molecular genetic tools available in this model organism.

Our approach is immediately compatible with a growing array of tools, based on SPT, to analyze local heterogeneity and spatiotemporal variation in mobility and binding states[28,29]. Under conditions in which photobleaching rates do not dominate turnover (e.g. low mobility and fast turnover as for GFP::Actin), it is possible to measure spatiotemporal variation in turnover directly from single particle trajectories. As an alternative, we introduced a new method called smPReSS that estimates bulk turnover rates by fitting single molecule counts vs time to kinetic exchange models. smPReSS relies only on single molecule detection and thus is insensitive to particle tracking errors. As illustrated by our analysis of Par-6 turnover, smPReSS can be tuned to measure turnover rates under conditions that are inaccessible to

SPT analysis or to ensemble-based measurements like FRAP and its variants. A key assumption underlying both approaches is that the kinetics remain stationary during the time it takes to measure them; the validity of this assumption must be assessed on a case-by-case basis.

Finally, we developed and optimized the methods described here for use in *C. elegans*. However sequence specific inhibition of GFP expression in transgenic strains expressing GFP fusions proteins could be implemented in other model organisms through a variety of methods, in particular RNA interference and targeted protein degradation. Likewise, the use of intrinsic turnover to sample single molecule dynamics is a general principle that could be readily applied in other organisms and cell types. Combining these methods with molecular genetic tools already available in model organisms offers a promising new avenue to study cell surface dynamics in developing embryos.

Online methods

(1) *C. elegans* culture and strains

We cultured *C. elegans* strains under standard conditions[37]. The GFP fusion strains used in this study are: GFP::Actin, JH1541, unc-119(ed4);pJH7.03 [unc-119; pie-1:GFP:actin::pie-1 3′UTR] (courtesy of Geraldine Seydoux); GFP::PAR-1, JH1734, unc-119(ed3); axIs1245[pAC2.01: pie-1::GFP::PAR-1::pie-1 3′UTR] (ref. 38); GFP:ANI-1, OD38, unc-119(ed3) III; ltIs28 [pASM14; pie-1::GFP-TEV-STAG::ani-1::pie-1 3′UTR; unc-119 (+)] (ref. 39); GFP:Utrophin, MG589, mgSi3[cb-UNC-119 (+) pie-1::GFP::UTROPHIN:::pie-1 3′UTR]II (3); PAR-6::GFP, FT17, xnIs3[par-6:PAR-6::GFP + unc-119(+)] (ref. 40); NMY-2::GFP, JJ1667: unc-119(ed3) III (ref. 41); zuIs115 [pKG47: nmy-2::gfp; unc-119(+)] I (courtesy of Jeremy Nance).

(2) RNA interference

We performed RNAi using the feeding method[42]. Bacteria targeting *nmy-2* were obtained from the feeding library of Kamath *et al.*[43]. The L4417 plasmid targeting the entire GFP sequence (generated by the Fire lab and available at http://www.addgene.org/1649/) was transformed into HT115(DE3) bacteria. Bacterial cultures for feeding were grown for 10–12 hours and then induced on standard nematode nutritional growth media plates containing 50 μg/ml Ampicillin and 1mM IPTG for 16–24 hours at 20–25°C. For *nmy-2(RNAi)*, L4 stage larvae were placed on feeding plates for 20–28 hours before imaging.

One potential issue with these experiments is that RNAi directed against GFP in strains expressing GFP fused to a given protein could lead to depletion of its endogenous counterpart through a transitive RNAi effect[44,45]. The transitive effect is directional, affecting C-terminal fusions only; because the PAR-6::GFP strain used in this study is a C-terminal fusion, there was a possibility that transitive RNAi could bias our results However, in every PAR-6::GFP embryo that we examined, we observed strong A-P patterning of residual Par-6::GFP when it was reduced to single molecule level and these embryos divided asymmetrically with a normal cleavage furrow position. To further verify the absence of a transitive depletion effect, we placed L4 hermaphrodites onto GFP RNAi plates for 24 h, transferred them as single worms to new GFP RNAi plates for > 48hr and then scored their

progeny for survival. In all cases (10/10), the worms made roughly normal brood sizes and 100% of their eggs hatched into L1 larvae.

(3) Imaging Conditions

We dissected one-cell embryos from gravid hermaphrodites and mounted them under #1.5 22mm square coverslips in 3.5 μl standard egg buffer (118 mM NaCl, 40 mM KCl, 3.4 mM CaCl2, 3.4 mM MgCl2, 5 mM Hepes, pH 7.4) containing ~100 uniformly-sized polystyrene beads (15.6 ± 0.03 μm diameter, Bangs labs, #NT29N) to achieve uniform compression of the embryo surface across experiments.

We performed near-TIRF imaging on an inverted Nikon Ti-E microscope, equipped with a motorized TIRF Illuminator, a CFI Apo 1.45NA 100x oil immersion TIRF objective (Nikon) and a Ti-ND6-PFS Perfect Focus unit. Laser illumination at 488 nm from a 50 mW solid-state Sapphire laser (Coherent) was delivered by fiber optics to the TIRF Illuminator. Images were magnified by 1.5X and collected on an Andor iXon3 897 EM-CCD camera, yielding a pixel size of 107 nm.

We controlled laser illumination angle and intensity and image acquisition using Metamorph software (Molecular Devices). For all experiments, we set the laser illumination angle to a standard value that was chosen empirically to approximately maximize signal intensity while maintaining ~even illumination across the field of view. For single particle tracking experiments, we collected images in streaming mode with continuous illumination at 20%–100% laser intensity (100% ~ 1.6 $\mu W.\mu m^{-2}$) with 30–100 ms exposures to achieve frame rates of 10–30 frames per second. In some experiments we varied the duty ratio of laser exposure by operating the system in time-lapse mode with fixed laser intensity and exposure time and varied the interval between exposures to systematically vary photobleaching rates.

(4) Tuning GFP levels to achieve single molecule densities

The quasi-steady state densities observed during imaging depend on the initial (unobserved) densities, photobleaching rates and the intrinsic exchange kinetics of the target molecule (see main text and below). Thus we determined the appropriate initial densities empirically for a given strain and experiment. We achieved these initial densities in two steps: First, we used RNAi directed against the GFP sequence to deplete the maternal pool of GFP-tagged protein. RNAi against maternal proteins typically yields an exponential decrease in the maternal protein with time of exposure[46]. We controlled the degree of depletion by synchronizing larvae and sampling embryos at different times after the initiation of feeding to identify times at which discrete diffraction-limited speckles were observed at the cell surface. The optimal time varied from 12–36 hours depending on transgene expression levels and relative abundance at the cell surface vs cytoplasm, but was relatively consistent across experiments for a given strain. In a second step, we further “pre-tuned” GFP densities using pulses of <10 s in epi-illumination mode at 100% laser power (~ 1.6 $\mu W.\mu m^{-2}$) until adequate density was reached.

(5) Assessing potential effects of compression, laser exposure, ad GFP tagging

Using photobleaching to reduce GFP-tagged protein levels from full to single molecule levels in one step resulted in arrested development. However, the laser exposure required to fine-tune densities by photobleaching, or that occurs during single molecule imaging, did not cause embryos to arrest. In all of our single molecule imaging experiments, we verified that embryos initiated and completed cytokinesis with normal timing (PAR-6::GFP; 18/18) or in the case of Myosin-depleted embryos expressing GFP::Actin, attempted cytokinesis with normal timing. To further confirm a lack of phototoxicity, we imaged embryos expressing single molecule levels of Par-6::GFP at 100% laser power continuously for 150 seconds and then scored for (a) normal progression to 4-cell stage and (b) hatching. We performed this experiment under two mounting conditions: with embryos mounted under coverslips supported by ~15 μm beads as in most of our experiments, and with embryos mounted on agar pads, which are slightly less compressed. We found that 100% of the embryos imaged with glass beads progressed normally to the 4-cell stage, but only 1/10 actually hatched. In contrast, we found that 10/10 embryos imaged on agar pads hatched as normal L1 larvae. Because the laser exposure is approximately the same in both mounting conditions, we conclude that the failure of embryos imaged with glass beads to hatch is not due to phototoxicity per se, but rather to the greater compression of embryos mounted with 15 μm glass beads, which may affect the physical relationship between blastomeres at later stages and thus signaling processes that underlie cell fate determination. It remains a possibility that the dynamics observed in compressed embryos are slightly altered relative to uncompressed embryos, and this should be taken into account in interpreting results obtained using this method.

Another potential issue to consider is the effects of the GFP tag itself on the observed single molecule dynamics. In the case of Par-6::GFP, we used a transgene that has been shown to rescue a null mutation in *par-6*, suggesting that the effects on observed dynamics is minimal. We have not verified functional rescue by GFP::Actin and thus the turnover rates measured with this probe may not be identical to the endogenous turnover rates for F-actin. This should have no bearing on the validity or accuracy of the methods we report here, and it should not alter our qualitative conclusions that both F-actin assembly and turnover are modulate spatially and temporally during cytokinesis, but it may affect the quantitative differences we report, and thus these should be interpreted with appropriate care.

(6) Verifying single molecule levels

Following Tokunaga *et al.*[20], we defined the intrinsic speckle intensity as the averaged intensity around the centroid of the particle over a 2 pixel radius minus the averaged background in a surrounding 2 pixels wide region. To measure the mean and standard deviation of the intrinsic intensity for single molecules (I_{mono} and σ_{mono}), we reduced GFP densities until the distribution of intrinsic speckle intensities no longer changed and then fit the distribution to a pure Gaussian. To estimate the distribution of speckle sizes (#GFP molecules/speckle) at higher densities as in Fig. 1f and Supplementary Fig. 3a), we fit the distribution of intrinsic speckle intensities to a sum of Gaussians $G=\sum_{k=1}^{n} w_k \cdot G(I_k, \sigma_k)$, where $G(I_k,\sigma_k)$ is a pure Gaussian with mean $I_k = k \cdot I_{mono}$ and standard deviation

$\sigma_k = \sqrt{k} \cdot \sigma_{mono}$. We found that n = 3 was sufficient to obtain good fits over the range of densities shown in Fig. 1f and Supplementary Fig. 3a. We performed all fits using Matlab's built-in fitting functions.

(7) Single molecule detection and tracking

We initially tested two different publicly available Matlab software packages for single particle detection and tracking: the Kilfoil (http://people.umass.edu/kilfoil/downloads.html) implementation of the Crocker-Grier algorithm[47,26] and uTrack[27] (http://lccb.hms.harvard.edu/software.html). In initial tests, both methods yielded very similar results for particle detection and tracking under the imaging conditions used here (average SNR ~ 5; single molecule densities such that trajectory mergers and splits are exceedingly rare; see Supplementary Table 1). Because the Kilfoil implementation of the Crocker-Grier method is significantly faster, we used it for all the analyses reported here.

In brief, the Crocker-Grier method localizes particles to sub-pixel resolution in individual frames by fitting local intensity peaks to a Gaussian point spread function. The two key detection parameters - peak and mean intensity of the candidate particles - are adjusted empirically for given imaging conditions using a graphical user interface. The particles are then linked frame-to-frame by minimizing the global displacement across all particles, given a user-chosen cutoff value for maximum particle displacement. A second parameter, the gap size, allows the possibility of ignoring "gaps" in a trajectory due to transient failures to detect particles. These transient failures occur mainly because motion blur causes the particle intensity to fall transiently below the detection threshold. We infer this because under identical imaging conditions and using identical detection parameters, slow moving PAR-6::GFP molecules (the "subdiffusive class in Figure 3) almost never fall below the detection threshold (see Supplementary Movie 5), while fast-diffusing PAR-6::GFP particles frequently escape detection (see Supplementary Movie 4).

For Par-6::GFP, which can be highly mobile and thus subject to motion blur (compare Supplementary Movies 4 and 5 which show fast and slow-moving Par-6::GFP molecules), we used a cutoff value r = 5 and a gap size of 7 frames, yielding a maximum gap time of t_{gap} = 231 ms. For these values, the probability of a molecule diffusing farther than r after a time t_{gap} $p(r,\Delta t) = 1 - e^{-r^2/(4D\cdot\Delta t)}$ (ref. 48), was less than 0.05, and the maximum allowed jump of 5 pixels was nearly an order of magnitude less than the average distance between single molecules (~40 pixels; see Supplementary Table 1), ensuring that false gap closures are extremely rare.

For GFP::Actin, we used a maximum step size cutoff value of 3 pixels and an allowable gap size of 0 frames to perform the tracking shown in Supplementary Table 1. For the data shown in Figure 4, to further improve tracking for estimates of turnover by SPT, we pre-averaged 10 frames before the initial detection step and then performed tracking on the averaged data, again with a step size cutoff of 3 pixels and a gap size of 0. Allowing gap sizes of 1 or 2 in the analysis of the time-averaged data resulted in 18% (gap size = 1) and 25% (gap size = 2) of trajectories with reconnection events, suggesting that as many as 25% of the appearance and disappearance events counted in the analysis with gap size = 0 could

be false. In principle, this could result in as much as a 25% overestimate of the *absolute* value of k_{off}. However, the fraction of trajectories with gaps was very similar at different axial positions (see Supplementary Figure 5), suggesting that failures to detect some gap closures will have minimal impact on the *relative* values we report in Figure 4.

We measured an upper bound on the axial (1D) localization precision by tracking Utrophin::GFP molecules in embryos arrested in meiosis. Under these conditions, Utrophin::GFP is bound to a highly immobile network of cortical microfilaments, and thus measuring the amplitude of position fluctuations should yield an upper bound on the axial localization precision for a probe that has the same signal-to-noise ratio as those used in our analysis of Actin and Par-6 dynamics. Following Huang *et al.*[49], we tracked each GFP molecule until it disappeared, resulting in iterative localization of 4784 molecules. Then we aligned *x* and *y* particle positions from each track by their centers-of-mass to generate generate distributions of x and y position fluctuations which we fit to a Gaussian function, yielding standard deviations of 24 ± 1 nm in *x* and *y* (Supplementary Fig. 6).

(8) Generation of simulated trajectories for comparison to Par-6 data

We simulated Brownian diffusion for a set of 177 particles with track lengths matching those for the 177 trajectories shown in Fig. 3b,c. For each trajectory, we selected at random a series of brownian steps, with mean size $\langle x \rangle = 4Dt$, where t = 33 ms was the interval between frames for the real data. Then we fit $MSD = 4Dt^{\alpha}$ for the first 10 lag times to obtain "estimates" for short term diffusivity and anomalous diffusion exponent α. For the data shown in Supplementary Fig. 4, we used a single value of D for all simulated particles, and we varied D from 0.1 to 0.6. For the simulated data shown in Fig. 3d, we assigned a normally distributed diffusion coefficient to each simulated particle, such that Dsim $\rightarrow \mathcal{N}$ (0.15,005).

Supplementary Material

Refer to Web version on PubMed Central for supplementary material.

Acknowledgments

This research was supported by the US National Institutes of Health R01 grant GM098441 (to EM). EM also acknowledges support from the University of Chicago Materials Research Science & Engineering Center. We would like to thank Geraldine Seydoux, Jeremy Nance, Ken Kemphues, Michael Glotzer and Katrina Longhini for strains, Anne Sailer for technical support, Nathan Bartley, Xiaolei Zhang and Wushi Dong for their contributions to the initial stages of this project, and the Glotzer lab for sharing strains and reagents.

References

1. Lord SJ, Lee HL, Moerner WE. Single-molecule spectroscopy and imaging of biomolecules in living cells. Anal Chem. 2010; 82:2192–203. [PubMed: 20163145]
2. Xia T, Li N, Fang X. Single-molecule fluorescence imaging in living cells. Annu Rev Phys Chem. 2013; 64:459–80. [PubMed: 23331306]
3. Sako Y, et al. Live cell single-molecule detection in systems biology. Wiley Interdiscip Rev Syst Biol Med. 2012; 4:183–92. [PubMed: 21913339]

4. Waterman-Storer CM, Desai A, Bulinski JC, Salmon ED. Fluorescent speckle microscopy, a method to visualize the dynamics of protein assemblies in living cells. Curr Biol. 1998; 8:1227–30. [PubMed: 9811609]
5. Ponti A, Machacek M, Gupton SL, Waterman-Storer CM, Danuser G. Two distinct actin networks drive the protrusion of migrating cells. Science. 2004; 305:1782–6. [PubMed: 15375270]
6. Watanabe N, Mitchison TJ. Single-molecule speckle analysis of actin filament turnover in lamellipodia. Science. 2002; 295:1083–6. [PubMed: 11834838]
7. Douglass AD, Vale RD. Single-molecule imaging of fluorescent proteins. Methods Cell Biol. 2008; 85:113–25. [PubMed: 18155461]
8. Douglass AD, Vale RD. Single-molecule microscopy reveals plasma membrane microdomains created by protein-protein networks that exclude or trap signaling molecules in T cells. Cell. 2005; 121:937–50. [PubMed: 15960980]
9. Millius A, Watanabe N, Weiner OD. Diffusion, capture and recycling of SCAR/WAVE and Arp2/3 complexes observed in cells by single-molecule imaging. J Cell Sci. 2012; 125:1165–76. [PubMed: 22349699]
10. Ueda M, Sako Y, Tanaka T, Devreotes P, Yanagida T. Single-molecule analysis of chemotactic signaling in Dictyostelium cells. Science. 2001; 294:864–7. [PubMed: 11679673]
11. Uyemura T, Takagi H, Yanagida T, Sako Y. Single-molecule analysis of epidermal growth factor signaling that leads to ultrasensitive calcium response. Biophys J. 2005; 88:3720–3730. [PubMed: 15749770]
12. Jaqaman K, et al. Cytoskeletal control of CD36 diffusion promotes its receptor and signaling function. Cell. 2011; 146:593–606. [PubMed: 21854984]
13. Giannone G, Hosy E, Levet F, Constals A, Schulze K, Sobolevsky AI, Rosconi MP, Gouaux E, Tampé R, Choquet D, Cognet L. Dynamic superresolution imaging of endogenous proteins on living cells at ultra-high density. Biophys J. 2010; 99:1303–10. [PubMed: 20713016]
14. Manley S, et al. High-density mapping of single-molecule trajectories with photoactivated localization microscopy. Nat Methods. 2008; 5:155–7. [PubMed: 18193054]
15. Burnette DT, et al. A role for actin arcs in the leading-edge advance of migrating cells. Nat Cell Biol. 2011; 13:371–81. [PubMed: 21423177]
16. Niu L, Yu J. Investigating intracellular dynamics of FtsZ cytoskeleton with photoactivation single-molecule tracking. Biophys J. 2008; 95:2009–16. [PubMed: 18390602]
17. Sarov M, et al. A genome-scale resource for in vivo tag-based protein function exploration in C. elegans. Cell. 2012; 150:855–66. [PubMed: 22901814]
18. Bird, AF.; Bird, J. The structure of nematodes. Academic Press; California: 1991.
19. Rappleye CA, Paredez AR, Smith CW, McDonald KL, Aroian RV. The coronin-like protein POD-1 is required for anterior-posterior axis formation and cellular architecture in the nematode caenorhabditis elegans. 1999; 13:2838–51.
20. Tokunaga M, Imamoto N, Sakata-Sogawa K. Highly inclined thin illumination enables clear single-molecule imaging in cells. Nat Methods. 2008; 5:159–61. [PubMed: 18176568]
21. Salbreux G, Charras G, Paluch E. Actin cortex mechanics and cellular morphogenesis. Trends Cell Biol. 2012; 22:536–45. [PubMed: 22871642]
22. Beers M, Kemphues K. Depletion of the co-chaperone CDC-37 reveals two modes of PAR-6 cortical association in C. elegans embryos. Development. 2006; 133:3745–54. [PubMed: 16943281]
23. Nakayama Y, Shivas JM, Poole DS, Squirrell JM, Kulkoski JM, Schleede JB, Skop AR. Dynamin participates in the maintenance of anterior polarity in the Caenorhabditis elegans embryo. Dev Cell. 2009; 16:889–900. [PubMed: 19531359]
24. Cheeks RJ, Canman JC, Gabriel WN, Meyer N, Strome S, Goldstein B. C. elegans PAR proteins function by mobilizing and stabilizing asymmetrically localized protein complexes. Curr Biol. 2004; 14:851–62. [PubMed: 15186741]
25. Goehring NW, Hoege C, Grill SW, Hyman AA. PAR proteins diffuse freely across the anterior-posterior boundary in polarized C. elegans embryos. J Cell Biol. 2011; 193:583–94. [PubMed: 21518794]

26. Pelletier V, Gal N, Fournier P, Kilfoil ML. Microrheology of microtubule solutions and actin-microtubule composite networks. Phys Rev Lett. 2009; 102:188303. [PubMed: 19518917]
27. Jaqaman K, et al. Robust single-particle tracking in live-cell time-lapse sequences. Nat Methods. 2008; 5:695–702. [PubMed: 18641657]
28. Monnier N, Guo SM, Mori M, He J, Lénárt P, Bathe M. Bayesian approach to MSD-based analysis of particle motion in live cells. Biophys J. 2012; 103:616–26. [PubMed: 22947879]
29. Persson F, Lindén M, Unoson C, Elf J. Extracting intracellular diffusive states and transition rates from single-molecule tracking data. Nat Methods. 2013; 10:265–9. [PubMed: 23396281]
30. Hoege C, Hyman AA. Principles of PAR polarity in *Caenorhabditis elegans* embryos. Nat Rev Mol Cell Biol. 2013; 14:315–22. [PubMed: 23594951]
31. Kumfer KT, Cook SJ, Squirrell JM, Eliceiri KW, Peel N, O'Connell KF, White JG. CGEF-1 and CHIN-1 regulate CDC-42 activity during asymmetric division in the Caenorhabditis elegans embryo. Mol Biol Cell. 2010; 21:266–77. [PubMed: 19923324]
32. Pollard TD. Mechanics of cytokinesis in eukaryotes. Curr Opin Cell Biol. 2010; 22:50–6. [PubMed: 20031383]
33. Guha M, Zhou M, Wang YL. Cortical actin turnover during cytokinesis requires myosin II. Curr Biol. 2005; 15:732–6. [PubMed: 15854905]
34. Murthy K, Wadsworth P. Myosin II-dependent localization and dynamics of F-actin during cytokinesis. Curr Biol. 2005; 15:724–31. [PubMed: 15854904]
35. Danuser G, Waterman-Storer CM. Quantitative fluorescent speckle microscopy of cytoskeleton dynamics. Annu Rev Biophys Biomol Struct. 2006; 35:361–87. [PubMed: 16689641]
36. Dickinson DJ, Ward JD, Reiner DJ, Goldstein B. Engineering the Caenorhabditis genome using Cas9-triggered homologous recombination. Nat Methods. 2013; 10:1028–34. [PubMed: 23995389]
37. Brenner S. The genetics of Caenorhabditis elegans. Genetics. 1974; 77:71–94. [PubMed: 4366476]
38. Motegi F, Zonies S, Hao Y, Cuenca AA, Griffin E, Seydoux G. Microtubules induce self-organization of polarized PAR domains in *Caenorhabditis elegans* zygotes. Nat Cell Biol. 2011; 13:1361–7. [PubMed: 21983565]
39. Tse YC, Werner M, Longhini KM, Labbe JC, Goldstein B, Glotzer M. RhoA activation during polarization and cytokinesis of the early *Caenorhabditis elegans* embryo is differentially dependent on NOP-1 and CYK-4. 2012; 23:4020–31.
40. Totong R, Achilleos A, Nance J. PAR-6 is required for junction formation but not apicobasal polarization in *C. elegans* embryonic epithelial cells. Development. 2007; 134:1259–68. [PubMed: 17314130]
41. Munro E, Nance J, Priess JR. Cortical flows powered by asymmetrical contraction transport PAR proteins to establish and maintain anterior-posterior polarity in the early *C. elegans* embryo. Dev Cell. 2004; 7:413–24. [PubMed: 15363415]
42. Timmons L, Fire A. Specific interference by ingested dsRNA. Nature. 1998; 395:854. [PubMed: 9804418]
43. Kamath RS. Systematic functional analysis of the *Caenorhabditis elegans* genome using RNAi. Nature. 2003; 421:231–7. [PubMed: 12529635]
44. Sijen T, Fleenor J, Simmer F, Thijssen KL, Parrish S, Timmons L, Plasterk RH, Fire A. On the role of RNA amplification in dsRNA-trigerred gene silencing. Cell. 2001; 107:465–76. [PubMed: 11719187]
45. Alder MN, Dames S, Gaudet J, Mango SE. Gene silencing in *Caenorhabditis elegans* by transitive RNA interference. RNA. 2003; 9:25–32. [PubMed: 12554873]
46. Oegema, K.; Hyman, AA. WormBook. 2006. Cell division; p. 1-40.
47. Crocker JC, Grier DGJ. Methods of Digital Video Microscopy for Colloidal Studies. Colloid Interface Sci. 1996; 179:298–310.
48. Saxton MJ. Lateral diffusion in an archipelago. Biophys J. 1993; 54:1766–178. [PubMed: 8369407]
49. Huang B, Wang W, Bates M, Zhuang X. Three-dimensional super-resolution imaging by stochastic optical reconstruction microscopy. Science. 2008; 319:810–3. [PubMed: 18174397]

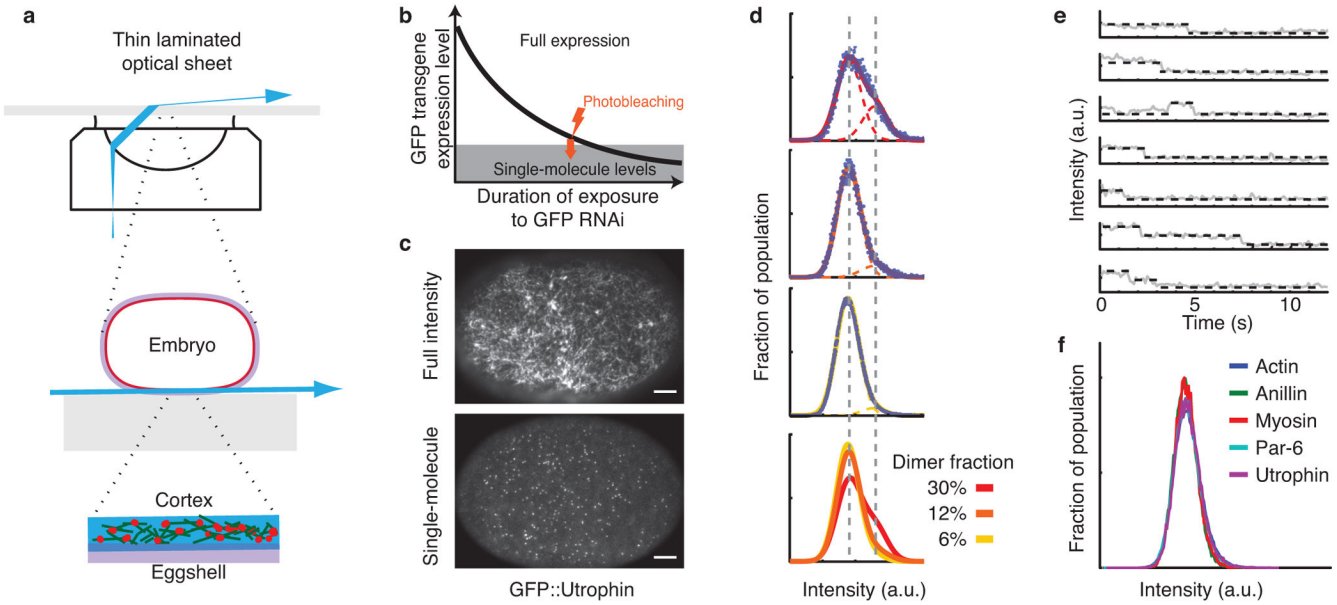

Figure 1. Imaging single molecules at the cortex in living embryos

(**a–c**) Schematic overview of the Near-TIRF imaging approach. (**a**) Top: Incident laser angle at the cover glass/specimen interface is tuned to create a thin and narrowly inclined laminar sheet (blue) of laser light. At cell (middle) and subcellular (bottom) scales, the laminar sheet is nearly parallel to the coverslip/specimen interface, and is thick enough to illuminate the entire cell cortex in the field of view. (**b**) Basic approach to achieve single-molecule levels for any GFP-fusion strain in *C. elegans*, using a combination of RNAi against GFP and photobleaching. (**c**) Near-TIRF micrographs of a one-cell embryo expressing GFP::Utrophin showing full intensity and single-molecule levels. Scale bar = 5 μm. (**d**) Distribution of intrinsic speckle intensities (average particle intensity – local average background) in a strain expressing GFP::PAR-1 for a range of depletion levels. Fits to a sum of two Gaussians representing one and two-molecule speckles measure a decrease in the proportion of doublets from 12% to 5%. Bottom panel compares directly all three previous panels. Images were obtained using identical imaging conditions. (**e**) Direct verification of single-molecule levels by single step photobleaching in an embryo expressing GFP::Actin. Multiple step photobleaching can be readily detected at higher expression levels (last two panels). (**f**) Intrinsic speckle intensity at low particle densities is essentially identical across all GFP strains tested.

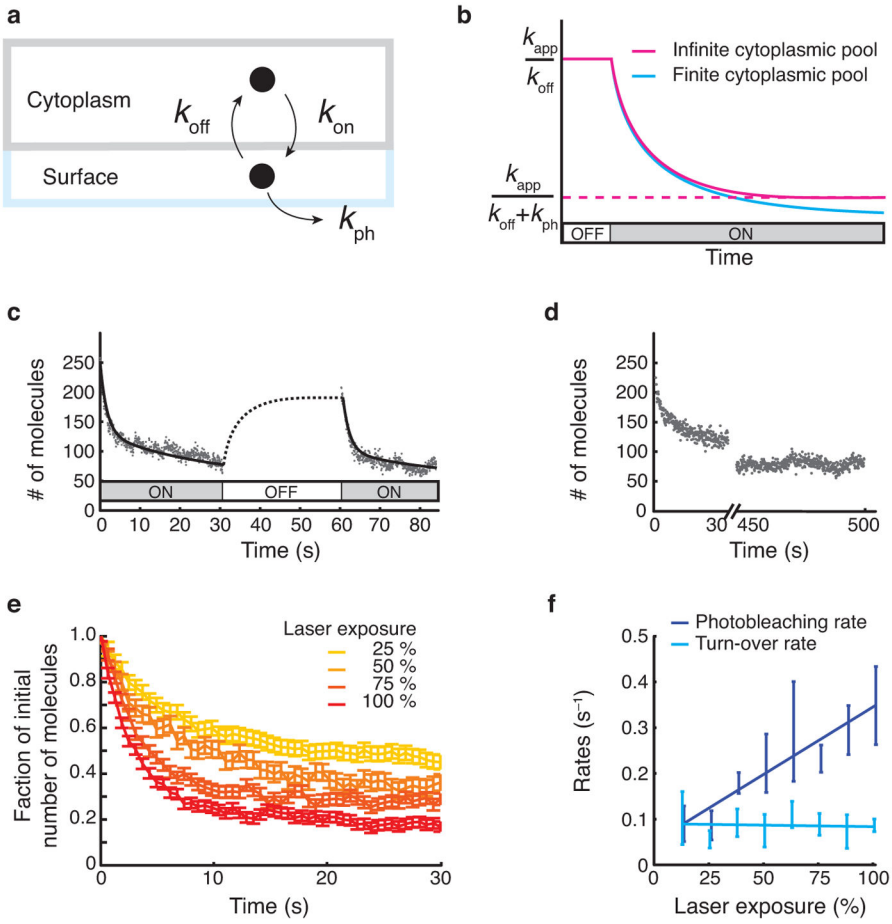

Figure 2. Exploiting dynamic exchange between cytoplasm and cell surface to obtain long-term tunable and high-density sampling of single molecule behaviors

(**a**) The basic kinetic principle: During imaging, the level of surface-associated proteins is set by a dynamic balance of: appearance (binding or assembly) at an observable rate k_{app}, disappearance (unbinding or disassembly) at a per-molecule rate k_{off}, and photobleaching at a per molecule rate k_{ph}. (**b**) The predicted response of an initially unobserved cell at steady state to a step change in illumination. For an infinite cytoplasmic pool, the surface density relaxes to a new illuminated steady state. For a finite cytoplasmic pool, fast relaxation is accompanied by a slower decay caused by irreversible photobleaching. (**c**) Biphasic response for GFP::Actin under illumination conditions that allow accurate single molecule detection and tracking. Discontinuous time from t = 30s to t = 450 s. (**d**) The fast relaxation to a quasi-stable density during illumination is rapidly reversed when the laser is turned off. (**e**) Surface density vs time at various laser exposures, shown as a fraction of the initial unobserved density. Error bars indicate standard error of the mean (n=7,9,6,7, low to high laser exposure). (**f**) Estimates of per molecule disappearance (k_{off}) and photobleaching (k_{ph}) rates as a function of laser exposure. Error bars indicate standard deviation, (n=12,7,8,9,7,6,7,7, low to high laser exposure). Solid lines show a linear regression against the data. k_{ph} increases linearly with laser exposure, while k_{off} remains constant. 100% laser power ~ 1.6 μW.μm^{-2}.

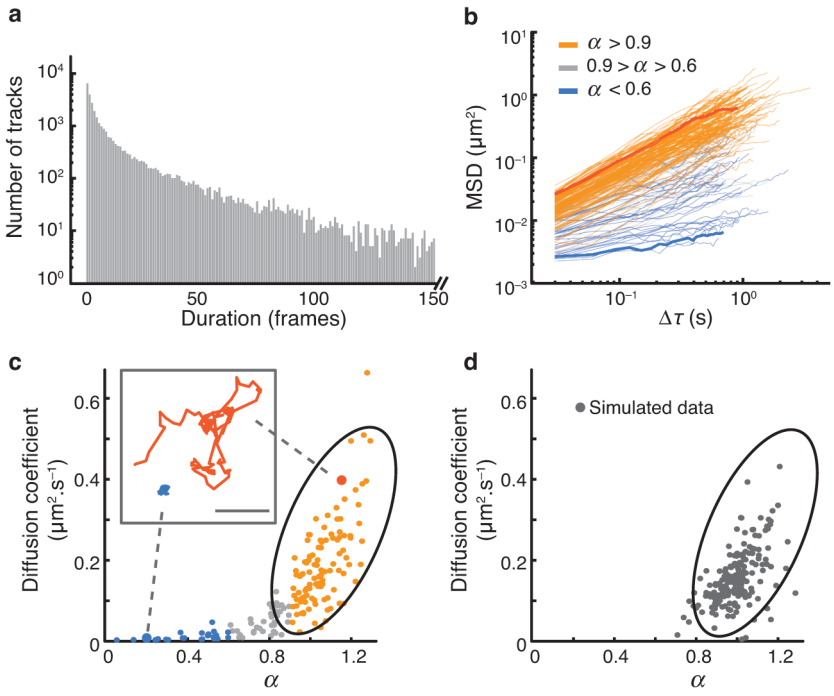

Figure 3. Analysis of PAR-6::GFP mobility during maintenance phase

(**a**) Distribution of track lengths for 30,558 tracks from n = 5 movies taken in one-cell embryos during maintenance phase. (**b**) Log/log plot of MSD versus lag time (Δτ) for all 177 tracks with length ≥ 80 frames extracted from one of the movies, reveals what appears to be a mixture of brownian and anomalous diffusion. Traces have been assigned colors based on slope (α). (**c**) Scatter plot of diffusion coefficient D versus exponent α, measured by fitting $MSD = 4Dt^{\alpha}$ for the first 10 lag times of the tracks shown in (**b**). Color scheme same as (**a**). Inset shows two particular trajectories drawn from opposite ends of the scatter plot and indicated by colored circles. Scale bar, 1 μm. (**d**) Scatter plot for 177 trajectories obtained by simulating pure brownian diffusion for ≥ 80 frames with $D = 0.15 \pm 0.05$ $\mu m^2.s^{-1}$ and measuring D and α as in (**c**). Note the close match to experimental data for $0.9 < \alpha < 1.2$, but the failure to match points at the bottom left (low D and α).

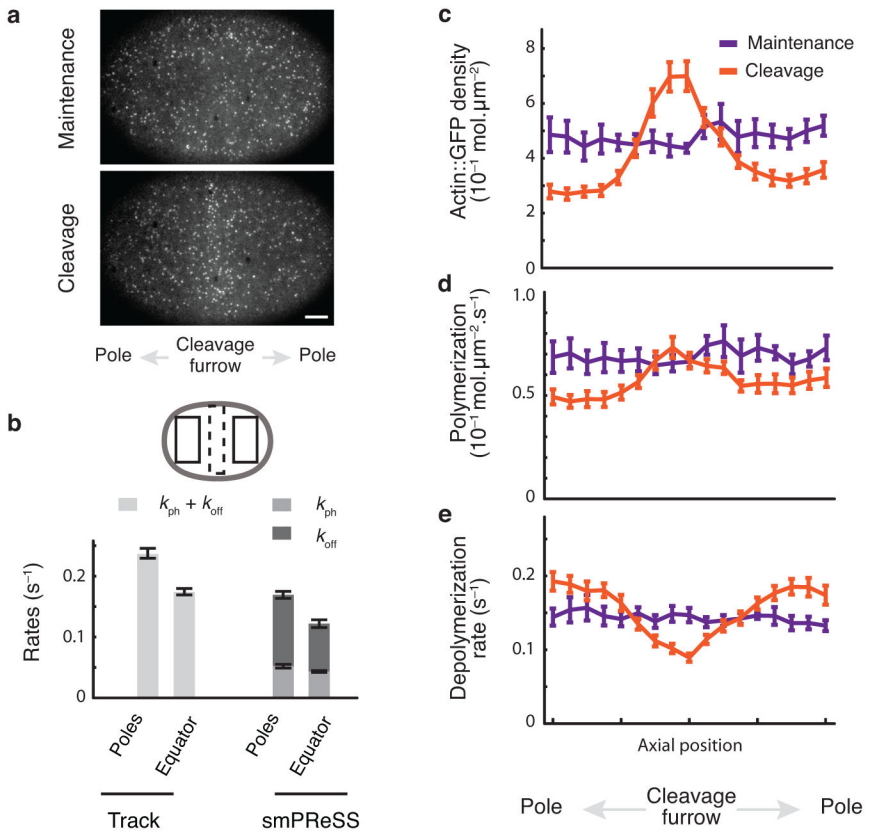

Figure 4. Spatial and temporal analysis of actin dynamics in *nmy-2 RNAi* embryos

(**a**) Near-TIRF micrographs of GFP::Actin during maintenance phase (top) and cleavage (bottom). (**b**) Measurements of turnover at the equator and poles during anaphase using tracking (left) or smPReSS (right). Schematic at top left indicates the equatorial (dashed box) and polar (solid box) regions in which the measurements were made. For tracking, the sum of k_{off} and k_{ph} is displayed; for smPReSS, the values for k_{ph} and k_{off} are stacked. (**c–e**) Spatial variation in actin density and turnover kinetics during maintenance phase and cleavage measured by tracking and binned along the antero-posterior axis. (**c**) Cortical density; (**d**) polymerization rate; (**e**) depolymerization rate (instantaneous disappearance rate minus estimated photobleaching rate). In **b–e**, error bars indicate cell-to-cell SEM (n=7, maintenance and n=16, cleavage). Scale bar, 5 µm.